JMEPEG (2012) 21:2085–2089
DOI: 10.1007/s11665-012-0133-3

1059-9495/$19.00

Preparation and Characterization of Ir Coating on WC Ceramic by Double Glow Plasma

Zhongwei Zhang, Zhenghui Xu, Jinming Wang, Wangping Wu, and Zhaofeng Chen

(Submitted November 8, 2010; in revised form July 5, 2011)

Dense and adherent Ir coating was deposited on porous WC ceramic by double glow plasma (DGP). There were two cathodes in the vacuum deposition chamber. The bias voltage of Ir target and WC substrate were −900 and −350 V, respectively. The Ir coating was characterized using scanning electron microscopy, x-ray diffraction, nanoindentation instrument, and scratch tester to examine the microstructure and the mechanical properties. The results indicated that the deposition rate by DGP was up to 5-6 μm/h which was faster than that by metal-organic chemical vapor deposition and magnetron sputtering. The Ir coating had a preferential growth orientation of (220) crystal face. The hardness was 800 HV. The elastic modulus was 644 GPa. The excellent mechanical properties were attributed to the preferential growth, the large compressive stress, and the shrinkage of the lattice parameters. The adhesive force was up to 51 N. The strong adhesion was attributed to the mechanical locking and chemical reaction between the Ir coating and the porous WC substrate.

Keywords double glow plasma, Ir coating, preferential growth orientation, WC ceramic

1. Introduction

Because of the extremely high melting point (2870 °C), high hardness (2242 HV), and relatively low coefficient of thermal expansion (CTE) (5.2×10^{-6} K), tungsten carbide (WC) ceramic had been used as molding core for preparing aspheric glass lens (Ref 1, 2). However, WC ceramic suffered from catastrophic oxidation at high temperature. Metallic iridium (Ir) coating was being researched to improve the precision grinding and anti-oxidizing of WC mold for the high melting point (2443 °C) and low oxygen permeability (less than 10^{-14} g/cm·s at 2200 °C) (Ref 3, 4). Ir coating could be prepared by various techniques, such as metal-organic chemical vapor deposition (MOCVD) (Ref 5-7), magnetron sputtering (MS) (Ref 8, 9), electro-chemical deposition (Ref 10, 11), laser-induced chemical decomposition (Ref 12), and slurry dipping (Ref 13, 14).

In this study, the double glow plasma (DGP) was investigated to develop the Ir-based noble metal coating. The aim was focused on the preparation and characterization of Ir coating on WC ceramic by DGP. Figure 1 shows the schematic diagram of DGP apparatus. Both the target and the substrate are used as the cathode electrodes. The argon was used as a working gas. After two different voltages were applied to the two-cathode electrodes, the target and substrate were surrounded by their own glow discharge. The substrate material was eroded by high-energy Ar^+ to clean the surface. The target material was eroded by the higher-energy Ar^+ to supply the sputtering atoms. The sputtering atoms traveled toward the surface of the substrate to form an excellent coating.

2. Experimental Process

An Ir plate (purity: 99.95%, ∅50 mm × 3.5 mm) was used as the target material. Some WC plates (15 mm × 15 mm × 2 mm) were used as the substrate materials. Argon was used as the working gas. Before deposition, the substrates were polished by metallographic abrasive paper.

The deposition parameters were base pressure 4×10^{-4} Pa, substrate temperature 850-900 °C, Ir target bias voltage −900 V, WC substrate bias voltage −350 V, working pressure 35 Pa, target/substrate spacing 15 mm, and deposition time 3 h.

The morphology was observed using scanning electron microscopy (SEM, Quanta 200, and FEI Co.). The phase identification was determined by x-ray diffraction (XRD, D8Advance, Bruker Co.) using Ni-filtered Cu-Kα radiation at a scanning rate of 0.5°/s scanning from 20° to 90° of 2θ. The residual stress was measured using x-ray diffractometer (XRD, XD-3A, Shimadz Co.) using Ni-filtered Cr-Kα radiation with a tilt angle ψ including 0°, 15°, 30°, and 45° for (220) plane of Ir crystals. The hardness and elastic modulus were estimated and calculated using nanoindentation instrument (DUH-W201, Shimadzu Co.). The adhesive force was measured by scratch tester (WS-2005).

Zhongwei Zhang, Department of Materials Science & Engineering, Tsinghua University, Beijing 100084, People's Republic of China; and National Key Laboratory of Advanced Functional Composite Materials, Aerospace Research Institute of Materials & Processing Technology, Beijing 100076, People's Republic of China; **Zhenghui Xu** and **Jinming Wang**, National Key Laboratory of Advanced Functional Composite Materials, Aerospace Research Institute of Materials & Processing Technology, Beijing 100076, People's Republic of China; and **Wangping Wu** and **Zhaofeng Chen**, College of Material Science and Technology, Nanjing University of Aeronautics and Astronautics, Nanjing 210016, People's Republic of China. Contact e-mail: zhaofeng_chen@163.com.

3. Results and Discussion

3.1 Microstructures of the Ir Coating

Figure 2 shows the SEM micrograph of the Ir coating. It was found that the coating was composed of a number of aggregates (See the dotted line rings). Each aggregate was composed of a number of finer stripy grains. No microcrack and other defects were observed on the surface.

Figure 3 shows the XRD pattern of the Ir coating. The diffraction pattern revealed that the Ir coating had a polycrystalline structure and a dominating (220) orientation. Some weak IrW diffraction peaks also appeared in the XRD pattern besides Ir peaks. It indicated that the interface reaction between Ir coating and WC substrate happened during deposition. The interface reaction was attributed to the high deposition temperature (850-900 °C). The chemical reaction followed the overall equation:

$$\mathrm{WC} + \mathrm{Ir} = \mathrm{IrW} + \mathrm{C} \quad \text{(Eq 1)}$$

According to the principle of the chemical reaction, the reaction products should include IrW and free C. However, the diffraction peak of the elemental C was absent in the XRD pattern.

The preferred orientation of the Ir coating was calculated with Haris method from the XRD results according to the following relationship (Ref 15):

$$\mathrm{TC} = \frac{I_i/I_0}{1/n\left[\Sigma_{i=1}^{n} I_i/I_0\right]} \quad \text{(Eq 2)}$$

where TC is the texture coefficient for a given plane, I_i is the actual intensity of measuring crystal plane, I_0 is the standard integrated intensity from the reference of American Society for Testing and Materials file, and n is the number of the diffraction peaks. TC values for (111), (200), (220), (311), and (222) peaks were calculated and shown in Table 1. The large difference among TC values indicated that the Ir crystals tended to have preferential growth orientation of (220) crystal plane. The lattice mismatch between WC (hexagonal structure, $a = 2.906$) and Ir (face-centered cubic (FCC), $a = 3.839$) was about 24%. Because the large mismatch could make the effect of the coherence energy at the interface negligible, the effect of the crystal structure of the WC substrate on the preferred orientation could be disregarded (Ref 16). It indicated that the preferred orientation could be attributed to the intrinsic characteristic of the DGP.

The (220) preferred orientation in DGP Ir coating is an interesting phenomenon. The preferred orientation could be related to the density of the broken metallic bond and the

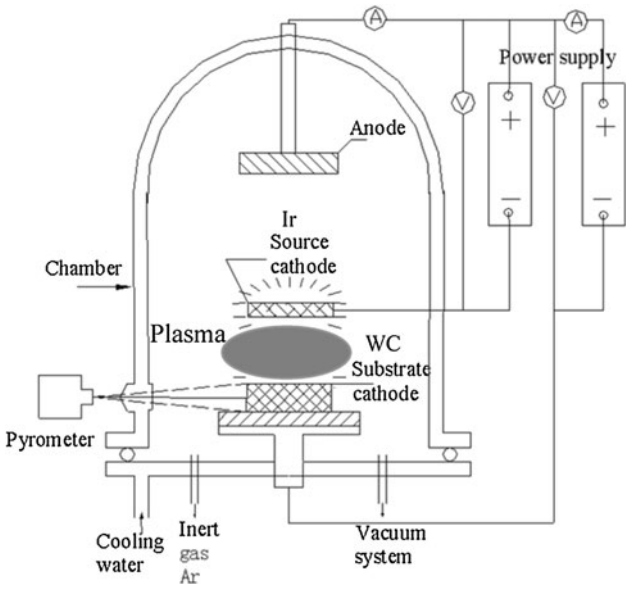

Fig. 1 Schematic diagram of DGP apparatus

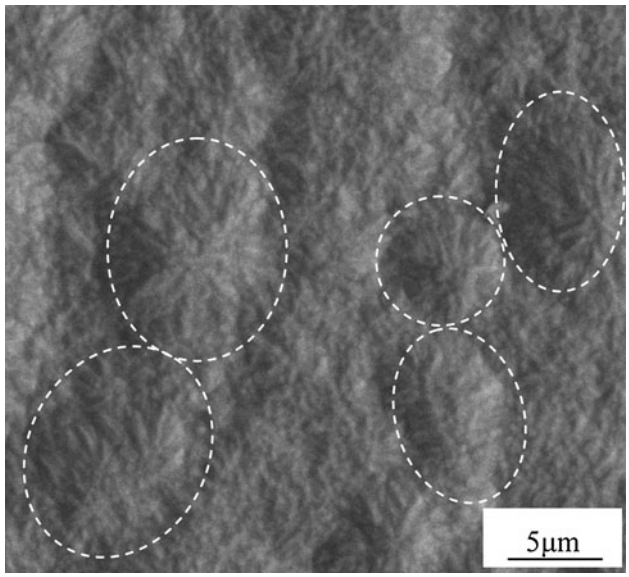

Fig. 2 SEM micrograph of the Ir coating

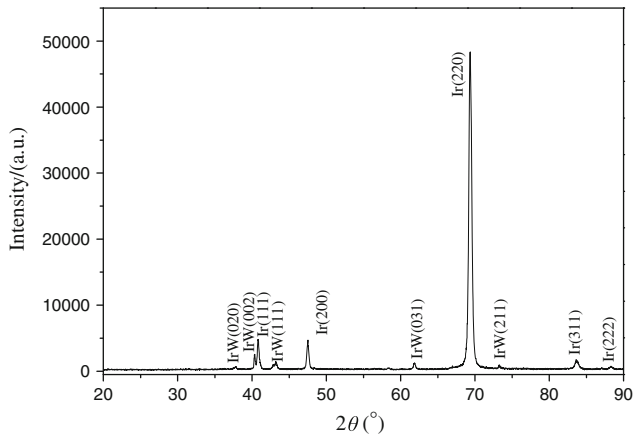

Fig. 3 XRD pattern of the Ir coating

Table 1 Texture coefficients of different crystal planes of Ir coating

	Crystal planes				
	(111)	(200)	(220)	(311)	(222)
I_0	100%	50%	40%	45%	15%
I_i	10%	10%	100%	3%	1%
TC	0.17	0.34	4.26	0.11	0.11

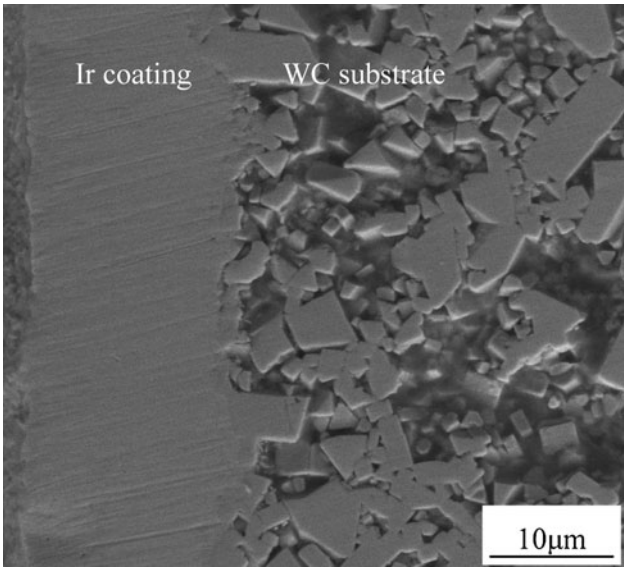

Fig. 4 SEM micrograph of the cross section of the Ir coating

relative surface energy of the dominate crystal faces of the crystal structure (Ref 17). Because the atom density of each crystal face was different, the density of the broken metallic bond was different when different crystal faces were split. The atom density and interplanar spacing of (111) crystal face were larger than other crystal faces in FCC crystal structure, and so the lowest energy was needed when (111) crystal face was pulled apart. The densities of the broken metallic bond of (111), (200), and (220) crystal faces in FCC crystal structure were $3.464/a^2$, $4/a^2$, and $4.242/a^2$ (where "a" denotes lattice parameter), respectively. If the (111) crystal face energy was assumed to be 1, then (200) crystal face energy and (220) crystal face energy should be 1.154 and 1.223, respectively. Because the (111) crystal face was close-packed, the (111) preferred orientation always appeared in MOCVD and PVD Ir coatings. During MOCVD and PVD, the as-deposited Ir atoms hardly suffered the bombardment from the high-energy ions. During DGP, however, the glow discharge around the substrate would make the as-deposited Ir atoms sputter continuously (re-sputter). Because the lower energy (200) crystal face and the lowest energy (111) crystal face were continuously destroyed, the euhedral crystal could not be obtained. The (220) crystal face just could be formed and grown up during DGP, which subsequently resulted in the preferential growth orientation of the Ir coating.

Figure 4 shows the SEM micrograph of the cross section of the Ir coating. The cross section was ground and polished by abrasive papers. Some parallel twills resulted from the sands appeared on the coating. It was found that the WC substrate was porous, and the Ir coating was dense. The interface between the WC substrate and the Ir coating exhibited excellent adhesion with no evidence of delamination and cracks. The Ir coating was about 15-18 μm in thickness. The average deposition rate was about 5-6 μm, which was faster than the deposition rates of MOCVD Ir coating (~0.5 μm/h) (Ref 18) and MS Ir coating (~0.9 μm/h) (Ref 19).

3.2 Properties of the Ir Coating

Figure 5 shows the diffraction spectrums of the Ir coating for different ψ angles. The peak shift indicated that the residual stress presented in the coating. Assuming that a biaxial stress state existed in the coating and the elastic properties of the Ir coating were isotropic, the residual stress could be calculated by the following relation (Ref 20):

$$\sigma = -\frac{\pi E_c \mathrm{ctg}\theta_0}{360(1+\upsilon_c)} \frac{\partial(2\theta)}{\partial(\sin^2\psi)} \quad \text{(Eq 3)}$$

where E_c is the Young's modulus of the metal Ir (540 GPa), υ_c is the Poisson's ratio of the metal Ir (0.246; Ref 21), ψ is the angle through which the sample is tilted, $2\theta_0$ is the Bragg angle of an Ir powder (144.99°), and 2θ is the Bragg angle of the as-prepared Ir coating. According to the above relation, the residual stress was −1.6 GPa. As we knew, the compressive stress in coating was helpful to improve the impact resistance, wear resistance, and crack resistance.

The lattice constants were calculated from the (220), (311), and (222) peaks of as-prepared Ir coating: a = 3.8328 Å, b = 3.8266 Å, and c = 3.8304 Å. However, $a = b = c$ = 3.8390 Å in the diffraction card of the Ir powder (JCPDS 6-0598). The shrinkage of the lattice parameters could largely be attributed to the compressive stress in Ir coating. According to the ion-peening mechanism (Ref 22), the growing coating was continuously and heavily struck by the high incoming energy ions to cause the densification, which led to the compressive stress. During DGP, the positive ions from the target electrode with the high kinetic energy were accelerated by the hybrid plasma to the substrate surface. The vigorous bombardment from the high-energy ions and particles could cause the high compressive stress in the coating.

In general, the residual stress in the coating was the sum of thermal stress, lattice mismatch, and intrinsic stress (Ref 23). The thermal stress was caused by thermal expansion mismatch between the substrate and the coating coupled with a change in temperature. The thermal stress σ_c could be calculated with the following formula (Ref 9):

$$\sigma_c = \frac{E_c(\alpha_s - \alpha_c)}{1-\upsilon_c}\Delta T \quad \text{(Eq 4)}$$

where E_c is the Young's modulus of the metal Ir, υ_c is the Poisson's ratio of the metal Ir, ΔT is the temperature difference between the deposition temperature and the measurement temperature, α_s is the CTE of the WC compound (5.2×10^{-6}/°C) (Ref 24), and α_c is the CTE of the metal Ir (6.2×10^{-6}/°C) (Ref 25). According to the formula (4), Ir coating on WC substrate would yield a tensile stress of about 0.63 GPa.

Lattice mismatch stress resulted from the substrate/coating epitaxial crystal relationship. The epitaxial growth did not happen during DGP compared to the diffraction patterns of the WC substrate and the Ir coating, so that the lattice mismatch stress would not be expected.

Without regard to lattice mismatch stress, the intrinsic stress in Ir coating would be the difference between the measured stress and the thermal stress (−2.23 GPa). The literature deemed that the intrinsic stress could arise from impurity atom incorporation, surface tension, phase changes, buried layer and gram boundary relaxation, chemical reaction, and energetic ion bombardment during deposition (Ref 26-28). According to chemical equation (1), IrW and C were the reaction products. Although the free carbon was not detected in XRD pattern, the free carbon atoms should be taken as impurity atoms within Ir coating. The experimental results indicated that the

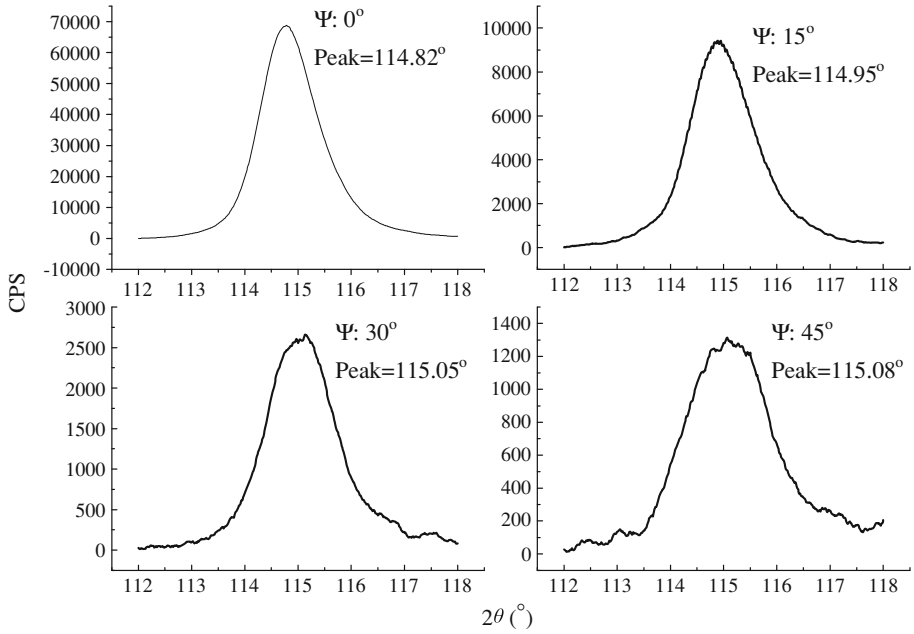

Fig. 5 Diffraction spectrums of the Ir coating for different ψ angle

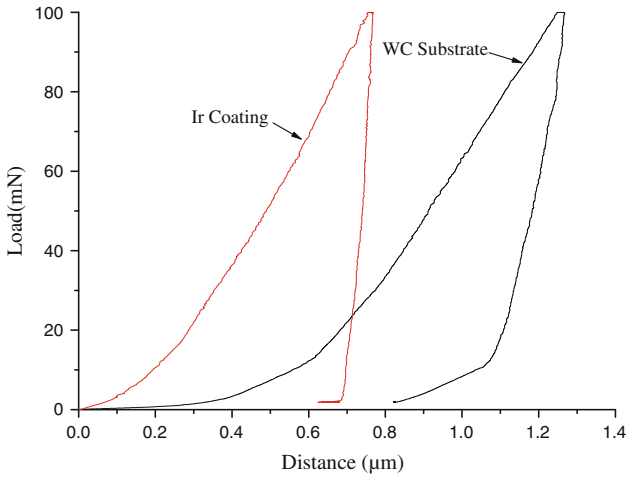

Fig. 6 Indentation force vs. indentation depth plots

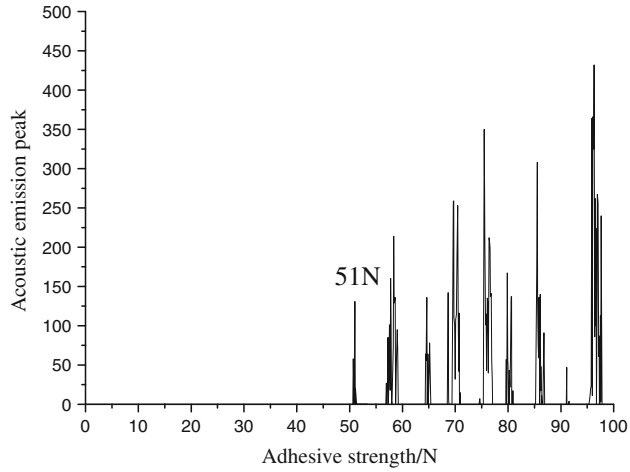

Fig. 7 Sound emission peak against the applied load according to the scratch test of Ir coating

intrinsic stress in Ir coating was mainly resulting from impurity atoms' incorporation, chemical reaction, and energetic ion bombardment.

Figure 6 shows the indentation load-depth curves of the Ir coating. The hardness and elastic modulus calculated from the load-depth curves were 800 HV and 644 GPa, respectively. The hardness of the Ir coating was higher than that of the bulk Ir (500 HV) (Ref 9). The elastic modulus of the Ir coating was higher than that of the bulk Ir (540 GPa) (Ref 21). When the load was 20 mN, the maximum indentation depth of the Ir coating was about 0.76 μm which was about 4.2-5.1% of the coating in thickness. Because the indentation depth did not exceed 10% of the thickness of the Ir coating, the effect of the WC substrate on the hardness and elastic modulus could be neglected. The high hardness was attributed to the preferred orientation growth of (220) crystal face and residual compressive stress. As we knew, the elastic modulus of the polycrystalline material was dependent on atom interaction, preferential orientation, temperature, and strain rate (Ref 29). The x-ray diffraction results indicated that all lattice parameters of the as-prepared Ir coating were less than that of the Ir powder. It was proved that the high elastic modulus was attributed to the contraction of the lattice parameter and the preferential orientation.

Figure 7 shows the sound emission peak against the applied load according to the scratch test. The adhesive force of the Ir coating was about 51 N. A general rule of thumb says (Ref 30) that a critical load of 30 N in scratch testing with a Rockwell C diamond tip is sufficient for sliding contact applications. The strong adhesion could result from the physical and chemical bondings. On the one hand, the pores near the surface of the substrate were fulfilled by Ir atoms to form mechanical locking between the substrate and the coating. On the other hand, the chemical reaction happened in the interface. The IrW compound played the role of the excellent binder between the coating and the substrate.

4. Conclusions

Dense and uniform Ir coating had been successfully obtained by DGP on WC ceramic. The Ir coating had the preferential growth orientation of the (220) crystal face. Because the density of the broken metallic bond of the (220) crystal face was large in FCC crystal structure, the (220) crystal face was not destroyed by the high-energy ions and the glow discharge.

The hardness and elastic modulus of the Ir coating were 800 HV and 644 GPa, respectively. The excellent mechanical properties were attributed to the preferential growth, the large compressive stress, and the shrinkage of the lattice parameters. The experimental results indicated that the intrinsic stress led to the compressive stress. The intrinsic stress was mainly attributed to impurity atoms' incorporation, chemical reaction, and energetic ion bombardment.

The adhesive force of the Ir coating was up to 51 N which was higher than the critical value. The strong adhesion was attributed to the mechanical locking and chemical reaction between the Ir coating and the porous WC substrate.

Acknowledgments

This study has been supported by the National Natural Science Foundation of China (50872055/E020703).

References

1. H.U. Kim, S.H. Jeong, H.J. Kim, and J.H. Kim, Optical Properties of Aspheric Glass Lens Using DLC Coating Mold, *Key Eng. Mater.*, 2007, **345-346**, p 1577–1580
2. H.U. Kim, S.H. Jeong, D.-K. Lee, S.-S. Kim, H.-J. Kim, and J.-H. Kim, A Study on Improvement of WC Core Surface Roughness by Feedrate Control, *J. Korean Soc. Precis. Eng.*, 2009, **26**(1), p 57–62
3. Y. Yamabemitarai, Platinum-Group-Metal-Based Intermetallics as High-Temperature Structural Materials, *JOM*, 2004, **56**(9), p 34–39
4. H.U. Kim, D.-H. Cha, H.-J. Kim, and J.-H. Kim, Rhenium-Iridium Coating Effect of Tungsten Carbide Mold for Aspheric Glass Lens, *Int. J. Precis. Eng. Manuf.*, 2009, **10**(3), p 19–23
5. I.K. Igumenov, N.V. Gelfond, N.B. Morozova, and H. Nizard, Overview of Coating Growth Mechanisms in MOCVD Processes as Observed in Pt Group Metals, *Chem. Vap. Depos.*, 2007, **13**, p 633–637
6. J.R. Vargas Garcia and T. Goto, Chemical Vapor Deposition of Iridium, Platinum, Rhodium and Palladium, *Mater. Trans.*, 2003, **44**, p 1717–1728
7. W.B. Yang, L.T. Zhang, Y.F. Hua, and L.F. Cheng, Thermal Stability of Iridium Coating Prepared by MOCVD, *Int. J. Refract. Met. Hard Mater.*, 2009, **27**, p 33–36
8. K. Mumtaz, J. Echigoya, and M. Taya, Preliminary Study of Iridium Coating on Carbon/Carbon Composites, *J. Mater. Sci.*, 1993, **28**(20), p 5521–5527
9. K. Mumtaz and J. Echigoya, RF Magnetron Sputtered Iridium Coatings on Carbon Structural Materials, *Mater. Sci. Eng. A*, 1993, **167**, p 187–195
10. A. Etenko, T. McKechnie, A. Shchetkovskiy, and A. Smirnov, Oxidation-Protective Iridium and Iridium-Rhodium Coatings Produced by Electrodeposition from Molten Salts, *ECS Trans.*, 2007, **3**, p 151–157
11. B.A. Macklin, F.R. Owens, and P.A. LaMar, Development of Improved Methods of Depositing Iridium Coatings on Graphite, AFML TR 67-195, 1967
12. L. Snell, A. Nelson, and P. Molian, A Novel Laser Technique for Oxidation-Resistant Coating of Carbon-Carbon Composite, *Carbon*, 2001, **39**, p 991–999
13. E.K. Ohriner, Processing of Iridium and Iridium Alloys-Methods from Purification to Fabrication, *Platinum Met. Rev.*, 2008, **52**(3), p 186–197
14. J.M. Criscione, H.F. Volk, and A.W. Smith, Protection of Graphite from Oxidation at 2100°C, *AIAA J.*, 1966, **4**, p 1791–1792
15. W. Sun, X. Xiong, B.Y. Huang, G.D. Li, H.B. Zhang, P. Xiao, Z.K. Chen, and X.L. Zheng, Preparation of ZrC Nano-Particles Reinforced Amorphous Carbon Composite Coating by Atmospheric Pressure Chemical Vapor Deposition, *Appl. Surf. Sci.*, 2009, **255**, p 7142–7146
16. J.P. Zhao, X. Wang, Z.Y. Chen, S.Q. Yang, T.S. Shi, and X.H. Liu, Overall Energy Model for Preferred Growth of TiN Films During Filtered Arc Deposition, *J. Phys. D Appl. Phys.*, 1997, **30**, p 5–12
17. Z. Zhao, C. Wang, M. Li, L. Wang, and L. Kong, The Effects of Pulsed Nd:YAG Laser Irradiation on Surface Energy of Copper, *Appl. Surf. Sci.*, 2006, **252**, p 4257–4263
18. F. Maury and F. Senocq, Iridium Coatings Grown by Metal-Organic Chemical Vapor Deposition in a Hot-Wall CVD Reactor, *Surf. Coat. Technol.*, 2003, **163-164**, p 208–213
19. F. Wu, W. Chen, J. Duh, Y. Tsai, and Y. Chen, Ir-Based Multi-Component Coating on Tungsten Carbide by RF Magnetron Sputtering Process, *Surf. Coat. Technol.*, 2003, **163-164**, p 227–232
20. W.L. Lia, W.D. Fei, and T. Hanabusa, Effect of Deposition Condition on Residual Stress of Iron Nitride Thin Films Prepared by Magnetron Sputtering and Ion Implantation, *Appl. Surf. Sci.*, 2006, **252**, p 2847–2852
21. Y. Huanga, F. Zhangb, K.C. Hwangb, W.D. Nix, G.M. Pharrd, and G. Feng, A Model of Size Effects in Nano-Indentation, *J. Mech. Phys. Solids*, 2006, **54**, p 1668–1686
22. V. Teixeira, Mechanical Integrity in PVD Coatings Due to the Presence of Residual Stresses, *Thin Solid Films*, 2001, **392**(2), p 276–281
23. A.J. McGinnis, T.R. Watkins, and K. Jagannadham, Residual Stresses in a Multilayer System of Coatings, *Int. Centre Diffr. Data*, 1999, **41**, p 443–454
24. P.K. Deshpande, J.H. Li, and R.Y. Lin, Infrared Processed Cu Composites Reinforced with WC Particles, *Mater. Sci. Eng. A*, 2006, **429**, p 58–65
25. J.J. Halvorson and R.T. Wimber, Thermal Expansion of Iridium at High Temperatures, *J. Appl. Phys.*, 1972, **43**, p 2519–2522
26. H. Windischmann, Intrinsic Stress in Sputter-Deposited Thin Films, *Crit. Rev Solid State Mater. Sci.*, 1992, **17**(6), p 547–596
27. O. Knotek, R. Elsing, G. Kramer, and F. Jungblutt, On the Origin of Compressive Stress in PVD Coatings—An Explicative Model, *Surf. Coat. Technol.*, 1991, **46**, p 265–274
28. C.A. Davis, A Simple Model for the Formation of Compressive Stress in Thin Films by Ion Bombardment, *Thin Solid Films*, 1993, **226**, p 30–34
29. M. Liu, B. Shi, J. Guo, X. Cai, and H. Song, Lattice Constant Dependence of Elastic Modulus for Ultrafine Grained Mild Steel, *Scripta Mater.*, 2003, **49**, p 167–171
30. S. Hogmark, S. Jacobson, and M. Larsson, Design and Evaluation of Tribological Coatings, *Wear*, 2000, **246**, p 20–33